

Polarized Line Formation in Arbitrary Strength Magnetic Fields :
the case of a two-level atom with hyperfine structure splitting

M. SAMPOORNA,¹ K. N. NAGENDRA,^{1,2} K. SOWMYA,³ J. O. STENFLO,^{2,4} AND L. S. ANUSHA³

¹*Indian Institute of Astrophysics, Koramangala, Bengaluru 560 034, India*

²*Istituto Ricerche Solari Locarno, Locarno Monti, Switzerland*

³*Max-Planck-Institut für Sonnensystemforschung, Justus-von-Liebig-Weg 3, 37077, Göttingen, Germany*

⁴*Institute for Particle Physics and Astrophysics, ETH Zurich, CH-8093 Zurich, Switzerland*

(Received; Revised; Accepted)

Submitted to ApJ

ABSTRACT

Quantum interference effects together with partial frequency redistribution (PFR) in line scattering produce subtle signatures in the so called Second Solar Spectrum (the linearly polarized spectrum of the Sun). These signatures are modified in the presence of arbitrary strength magnetic fields via the Hanle, Zeeman, and Paschen-Back effects. In the present paper we solve the problem of polarized line formation in a magnetized atmosphere taking into account scattering in a two-level atom with hyperfine structure splitting together with PFR. To this end we incorporate the collisionless PFR matrix derived in Sowmya et al. (2014) in the polarized transfer equation. We apply the scattering expansion method to solve this transfer equation. We study the combined effects of PFR and Paschen-Back effect on polarized line profiles formed in an isothermal one-dimensional planar atmosphere. For this purpose, we consider the cases of D₂ lines of Li I and Na I.

Keywords: atomic processes - Sun: magnetic fields - line: formation - line: transfer - scattering - polarization

1. INTRODUCTION

The polarized spectra emanating from solar/ stellar atmospheres provide us with a unique diagnostic tool to unravel the underlying scattering physics and to detect the solar/ stellar magnetic fields. Therefore it is of utmost importance to solve the problem of polarized line formation in a magnetized atmosphere. In the present paper we consider this problem for the case of a two-level atom with unpolarized lower level and with hyperfine structure splitting (HFS).

When a radiating atom possesses a non-zero nuclear spin (I_s), the fine structure states of the atom (designated by the total electronic angular momentum quantum number J) undergo hyperfine structure splitting. The $J - I_s$ coupling results in hyperfine structure states labeled by F quantum number. The F states belong-

ing to a given J state can interfere resulting in the so called F -state interference. The problem of polarized line formation including this F -state interference and partial frequency redistribution (PFR) in the non-magnetic case has been dealt with in Fluri et al. (2003); Holzreuter et al. (2005); Smitha et al. (2012, 2013, 2014); Supriya et al. (2013b); Belluzzi & Trujillo Bueno (2013), and in Belluzzi et al. (2015). In the non-magnetic case, it is well-known that HFS causes a depolarization in the line core. In the presence of magnetic fields, the hyperfine structure F states further split into magnetic substates. When the magnetic splitting is much smaller than the HFS, we are in the linear Hanle-Zeeman regime, wherein the magnetic splitting varies linearly with the field strength. When the magnetic splitting becomes comparable to or larger than the HFS, we enter the so-called incomplete Paschen-Back effect (PBE) regime. This field strength regime is characterized by non-linear splitting of the magnetic substates, the level-crossing, and anti-level crossing effects. With a further increase in the field strength, we

enter the complete PBE regime, wherein the magnetic splitting again varies linearly with field strength. The different field strength regimes produce interesting signatures in the singly scattered polarized line profiles (see [Bommier 1980](#); [Landi Degl’Innocenti & Landolfi 2004](#); [Belluzzi et al. 2007](#); [Sowmya et al. 2014, 2015](#)). Here we investigate the influence of PBE and PFR on Stokes profiles generated by multiple scattering in a magnetized atmosphere.

A PFR matrix for scattering on a two-level atom with non-zero nuclear spin (I_s) and in the presence of arbitrary magnetic fields has been derived for the collisionless case in [Landi Degl’Innocenti et al. \(1997\)](#) using a metalevel formalism and in [Sowmya et al. \(2014\)](#) using a Kramers-Heisenberg scattering approach ([Stenflo 1994](#)). This PFR matrix takes into account Hanle, Zeeman, and PBE regimes of field strength. In the present paper we include this PFR matrix in the polarized transfer equation and present a numerical method of solution. The corresponding collisional PFR matrix is given in [Bommier \(2017\)](#). Since the computation of the PFR matrix in the PBE regime is computationally expensive, we limit ourselves to the collisionless case. Furthermore, we consider the angle-averaged version of the magnetic PFR functions.

Solving the problem of the transfer of polarized spectral line radiation in the presence of arbitrary magnetic fields and including PFR is computationally a complex task. [Sampoorna et al. \(2008\)](#) generalized the perturbation method of [Nagendra et al. \(2002\)](#) to solve this problem for a two-level atom without HFS. More recently, an accelerated lambda iteration (ALI) method to solve the same problem is presented in [Alsina Ballester et al. \(2017\)](#) and [Sampoorna et al. \(2017\)](#). An iterative method based on classical lambda iteration to solve the polarized PFR line transfer equation in arbitrary fields for a two-term atom without HFS is presented in [del Pino Alemán et al. \(2016\)](#). In the present paper we apply the so-called scattering expansion method of [Frisch et al. \(2009\)](#) to solve the problem at hand. For our numerical studies we consider a one-dimensional isothermal constant property medium. We consider a two-level atom with upper level $J_b = 3/2$ and lower level $J_a = 1/2$ and with a nuclear spin $I_s = 3/2$, which is representative of Na I D₂ line. We also consider the Li I D₂ line case (which also corresponds to $J = 3/2 \rightarrow 1/2$ transition), wherein, $I_s = 1$ for ⁶Li isotope and $I_s = 3/2$ for ⁷Li isotope. For these two lines, we investigate the role played by the PBE, PFR, and radiative transfer.

In Section 2, we present the governing equations of the problem at hand. The scattering expansion method is

presented in Section 3. Numerical results are presented in Section 4. Conclusions are drawn in Section 5.

2. THE GOVERNING EQUATIONS

The polarized line radiative transfer equation in a planar atmosphere permeated by arbitrary magnetic fields \mathbf{B} is given by

$$\mu \frac{\partial}{\partial \tau} \mathbf{I}(\tau, x, \mathbf{n}) = \mathbf{K} \mathbf{I}(\tau, x, \mathbf{n}) - \mathbf{S}(\tau, x, \mathbf{n}). \quad (1)$$

Here $d\tau = -k_L^A dz$ is the line integrated vertical optical depth scale, $x = (\nu_{J_b J_a} - \nu) / \Delta\nu_D$ is the spectral distance from the line-center frequency $\nu_{J_b J_a}$ (corresponding to a $J_b \rightarrow J_a$ transition in the absence of HFS and magnetic fields) in Doppler width ($\Delta\nu_D$) units, $\mathbf{n}(\vartheta, \varphi)$ is the propagation direction of the ray (where ϑ is the inclination and φ is the azimuth defined with respect to the atmospheric normal), $\mu = \cos \vartheta$, and the Stokes vector $\mathbf{I} = [I, Q, U, V]^T$. The frequency integrated line absorption coefficient is defined as

$$k_L^A = \frac{h \nu_{J_b J_a}}{4\pi} N_a B(J_a I_s \rightarrow J_b I_s), \quad (2)$$

where N_a is the population of the lower level, h is the Planck constant, and B is the Einstein coefficient for absorption. The total absorption matrix is given by

$$\mathbf{K} = \mathbf{\Phi} + r \mathbf{E}, \quad (3)$$

where \mathbf{E} is the 4×4 unity matrix and r is the ratio of continuum to line averaged opacity. The 4×4 line absorption matrix $\mathbf{\Phi}$ is given by

$$\mathbf{\Phi}(x, \mathbf{n}) = \begin{pmatrix} \varphi_I & \varphi_Q & \varphi_U & \varphi_V \\ \varphi_Q & \varphi_I & \chi_V & -\chi_U \\ \varphi_U & -\chi_V & \varphi_I & \chi_Q \\ \varphi_V & \chi_U & -\chi_Q & \varphi_I \end{pmatrix}. \quad (4)$$

For a two-level atom with HFS and with unpolarized lower level, the absorption coefficients φ_i with $i = 0, 1, 2, 3$ (corresponding to $I, Q, U,$ and V) and anomalous dispersion coefficients χ_i with $i = 1, 2, 3$ (corresponding to $Q, U,$ and V) can be found in [Landi Degl’Innocenti & Landolfi \(2004\)](#). However these coefficients are usually given in a frame where the magnetic field is along the Z -axis. For the transfer computations, they need to be transformed to a frame where the Z -axis is along the atmospheric normal. Such a transformation is described in Appendix B of [Sampoorna et al. \(2017\)](#). The resulting coefficients are then given by

$$\varphi_i(x, \mathbf{n}) = \sum_{KQ} \mathcal{T}_Q^K(i, \mathbf{n}) e^{-iQ\varphi_B} d_{Q0}^K(\vartheta_B) \Phi_0^{0K}(J_a, J_b, x), \quad (5)$$

$$\chi_i(x, \mathbf{n}) = \sum_{KQ} \mathcal{T}_Q^K(i, \mathbf{n}) e^{-iQ\varphi_B} d_{Q0}^K(\vartheta_B) \Psi_0^{0K}(J_a, J_b, x), \quad (6)$$

where ϑ_B and φ_B are the inclination and azimuth of the magnetic field with respect to the atmospheric normal. The symbol $d_{QQ'}^K(\vartheta_B)$ stands for reduced rotation matrices, which are tabulated in Table 2.1 of Landi Degl'Innocenti & Landolfi (2004). $\mathcal{T}_Q^K(i, \mathbf{n})$ are the irreducible spherical tensors with $K = 0, 1, 2$ and $-K \leq Q \leq +K$ (see Landi Degl'Innocenti 1984). In analogy with the case of two-level atom without HFS we refer to Φ_0^{0K} and Ψ_0^{0K} as the generalized profile function and generalized dispersion profile function respectively, but now they are defined for the case of a two-level atom with HFS. They are given by

$$\begin{aligned} \Phi_0^{0K}(J_a, J_b, x) &= \frac{1}{2I_s + 1} \sqrt{3(2K + 1)} \sum_{i_a i_b F_a F_a' F_b F_b'} \\ &\times \sum_{m_a m_b q} (-1)^{q+1} \sqrt{(2F_a + 1)(2F_a' + 1)(2F_b + 1)} \\ &\times \sqrt{(2F_b' + 1)} C_{F_a}^{i_a} (J_a I_s, m_a) C_{F_a'}^{i_a} (J_a I_s, m_a) \\ &\times C_{F_b}^{i_b} (J_b I_s, m_b) C_{F_b'}^{i_b} (J_b I_s, m_b) \begin{Bmatrix} J_a & J_b & 1 \\ F_b & F_a & I_s \end{Bmatrix} \\ &\times \begin{Bmatrix} J_a & J_b & 1 \\ F_b' & F_a' & I_s \end{Bmatrix} \begin{pmatrix} F_b & F_a & 1 \\ -m_b & m_a & -q \end{pmatrix} \begin{pmatrix} F_b' & F_a' & 1 \\ -m_b & m_a & -q \end{pmatrix} \\ &\times \begin{pmatrix} 1 & 1 & K \\ q & -q & 0 \end{pmatrix} H(a, x_{ba}), \end{aligned} \quad (7)$$

and

$$\Psi_0^{0K}(J_a, J_b, x) = \Phi_0^{0K}(J_a, J_b, x) \{H(a, x_{ba}) \rightarrow F(a, x_{ba})\}. \quad (8)$$

Here m denotes the magnetic quantum number, and $\{H(a, x_{ba}) \rightarrow F(a, x_{ba})\}$ means that the $H(a, x_{ba})$ in Eq. (7) should be replaced by $F(a, x_{ba})$ in Eq. (8). In the incomplete PBE regime, the magnetic field produces a mixing of the F -states belonging to a given J , so that F is no longer a good quantum number. Thus the basis vectors in the incomplete PBE regime are denoted by $|JI_s im\rangle$, where the symbol i labels the different states spanned by the quantum numbers (J, I_s, m) . The symbol $C_F^i(JI_s, m)$ denotes the expansion coefficients corresponding to the expansion of the incomplete PBE regime basis vectors $|JI_s im\rangle$ on to the linear Hanle-Zeeman regime basis vectors $|JI_s Fm\rangle$ (see e.g., Eq. (11) of Sowmya et al. 2014). They are obtained by diagonalizing the magnetic Hamiltonian in the incomplete PBE regime (see Landi Degl'Innocenti & Landolfi 2004, also Sowmya et al. 2014). We remark that, Eqs. (7) and (8) correspond to the observer's reference frame,

wherein the Doppler motion of atoms through a convolution of the Maxwellian velocity distribution with the atomic frame profile function has been accounted for. Thus, in these equations, $H(a, x_{ba})$ and $F(a, x_{ba})$ denote respectively the magnetically shifted Voigt and Faraday-Voigt functions, wherein a is the damping parameter and $x_{ba} = (\nu_{i_b m_b, i_a m_a} - \nu) / \Delta\nu_D$ with $\Delta\nu_D$ the Doppler width and $\nu_{i_b m_b, i_a m_a}$ the line center frequency for $i_b m_b \rightarrow i_a m_a$ transition and it is defined as

$$\begin{aligned} \nu_{i_b m_b, i_a m_a} &= \nu_{J_b I_s i_b m_b, J_a I_s i_a m_a} \\ &= \nu_{J_b J_a} + \frac{E_{i_b}(J_b I_s, m_b) - E_{i_a}(J_a I_s, m_a)}{h}. \end{aligned} \quad (9)$$

Here E is the energy shift of a magnetic substate measured with respect to the energy of the parent J state (see Sowmya et al. 2014, for details on the way the energy shifts are calculated).

The source vector $\mathbf{S}(\tau, x, \mathbf{n})$ appearing in Eq. (1) is given by

$$\mathbf{S}(\tau, x, \mathbf{n}) = (r\mathbf{E} + \epsilon\Phi) B_{\nu_{J_b J_a}} \mathbf{U} + \mathbf{S}_{\text{scat}}(\tau, x, \mathbf{n}). \quad (10)$$

Here, $B_{\nu_{J_b J_a}}$ is the Planck function, $\mathbf{U} = [1, 0, 0, 0]^T$, and

$$\begin{aligned} \mathbf{S}_{\text{scat}}(\tau, x, \mathbf{n}) &= (1 - \epsilon) \\ &\times \oint \frac{d\mathbf{n}'}{4\pi} \int_{-\infty}^{+\infty} dx' \mathbf{R}(x, \mathbf{n}, x', \mathbf{n}', \mathbf{B}) \mathbf{I}(\tau, x', \mathbf{n}'), \end{aligned} \quad (11)$$

where ϵ is the thermalization parameter. In the absence of elastic collisions the redistribution matrix \mathbf{R} is simply given by the type-II redistribution matrix \mathbf{R}^{II} . For a two-level atom with HFS and in the PBE regime this matrix is given in Eq. (16) of Sowmya et al. (2014). However it is defined in a frame where the magnetic field is along the Z -axis. As described in Appendix A of Sampoorna et al. (2017), we transform this matrix to the atmospheric reference frame (where Z axis is along the atmospheric normal). The ij th element of this matrix then takes the form

$$\begin{aligned} R_{ij}^{\text{II}}(x, \mathbf{n}, x', \mathbf{n}', \mathbf{B}) &= \sum_{KQ} \mathcal{T}_Q^K(i, \mathbf{n}) \sum_{K'Q'} \\ &\times N_{QQ', \text{II}}^{K, K'}(x, x', \Theta, \mathbf{B}) (-1)^{Q'} \mathcal{T}_{-Q'}^{K'}(j, \mathbf{n}'), \end{aligned} \quad (12)$$

where $\mathbf{n}(\vartheta, \varphi)$ and $\mathbf{n}'(\vartheta', \varphi')$ refer respectively to the scattered and incident ray directions with respect to the atmospheric normal, and Θ denotes the scattering angle between the incident and scattered rays. The type-II magnetic kernel has the form

$$\begin{aligned} N_{QQ', \text{II}}^{K, K'}(x, x', \Theta, \mathbf{B}) &= e^{i(Q' - Q)\varphi_B} \sum_{Q''} d_{QQ''}^K(\vartheta_B) \\ &\times \mathcal{R}_{Q'', \text{II}}^{K, K'}(x, x', \Theta, B) d_{Q''Q'}^{K'}(-\vartheta_B). \end{aligned} \quad (13)$$

The PFR functions $\mathcal{R}_{Q'',\text{II}}^{K,K'}(x, x', \Theta, B)$ for the case of a two-level atom with HFS and in the PBE regime are given by

$$\begin{aligned}
\mathcal{R}_{Q'',\text{II}}^{K,K'}(x, x', \Theta, B) &= \frac{3(2J_b + 1)}{(2I_s + 1)} \sum_{i_a m_a i_f m_f i_b m_b i_{b'} m_{b'}} \\
&\times \sqrt{(2K + 1)(2K' + 1)} \cos \beta_{i_{b'} m_{b'} i_b m_b} e^{i\beta_{i_{b'} m_{b'} i_b m_b}} \\
&\times [(h_{i_b m_b, i_{b'} m_{b'}}^{\text{II}})_{i_a m_a i_f m_f} + i(f_{i_b m_b, i_{b'} m_{b'}}^{\text{II}})_{i_a m_a i_f m_f}] \\
&\times \sum_{F_a F_{a'}, F_f F_{f'}, F_b F_{b'}, F_{b' F_{b''}}, q q' q'' q'''} (-1)^{q - q'' + Q''} \\
&\times \sqrt{(2F_a + 1)(2F_f + 1)(2F_{a'} + 1)(2F_{f'} + 1)} \\
&\times \sqrt{(2F_b + 1)(2F_{b'} + 1)(2F_{b''} + 1)(2F_{b'''} + 1)} \\
&\times C_{F_f}^{i_f}(J_a I_s, m_f) C_{F_{f'}}^{i_{f'}}(J_a I_s, m_{f'}) C_{F_a}^{i_a}(J_a I_s, m_a) \\
&\times C_{F_{a'}}^{i_{a'}}(J_a I_s, m_{a'}) C_{F_b}^{i_b}(J_b I_s, m_b) C_{F_{b''}}^{i_{b''}}(J_b I_s, m_{b''}) \\
&\times C_{F_{b'''}}^{i_{b'''}}(J_b I_s, m_{b'''}) C_{F_{b''''}}^{i_{b''''}}(J_b I_s, m_{b''''}) \begin{Bmatrix} J_a & J_b & 1 \\ F_b & F_f & I_s \end{Bmatrix} \\
&\times \begin{Bmatrix} J_a & J_b & 1 \\ F_{b'} & F_{f'} & I_s \end{Bmatrix} \begin{Bmatrix} J_a & J_b & 1 \\ F_{b''} & F_a & I_s \end{Bmatrix} \begin{Bmatrix} J_a & J_b & 1 \\ F_{b'''} & F_{a'} & I_s \end{Bmatrix} \\
&\times \begin{pmatrix} F_b & F_f & 1 \\ -m_b & m_f & -q \end{pmatrix} \begin{pmatrix} F_{b'} & F_{f'} & 1 \\ -m_{b'} & m_{f'} & -q' \end{pmatrix} \begin{pmatrix} F_{b''} & F_a & 1 \\ -m_b & m_a & -q'' \end{pmatrix} \\
&\times \begin{pmatrix} F_{b'''} & F_{a'} & 1 \\ -m_{b'''} & m_{a'} & -q''' \end{pmatrix} \begin{pmatrix} 1 & 1 & K \\ q & -q' & Q'' \end{pmatrix} \begin{pmatrix} 1 & 1 & K' \\ q''' & -q'' & -Q'' \end{pmatrix}. \quad (14)
\end{aligned}$$

The auxiliary functions h^{II} and f^{II} are defined in Equations (18)–(22) of Sowmya et al. (2014). All the different symbols and quantities appearing in the above equation can be found in the same reference. We recall that Eq. (14) is defined in the observer's reference frame, wherein the effects of Doppler redistribution have been account for.

From Eq. (1) it is clear that all the four Stokes parameters are coupled to each other. We apply the DELOPAR method of Trujillo Bueno (2003, see also Sampoorna et al. 2008) to obtain a formal solution of such a coupled first order ordinary differential equation.

3. SCATTERING EXPANSION METHOD

Frisch et al. (2009) presented an iterative method to solve the problem of polarized line formation in weak magnetic fields. This method is based on the Neumann series expansion of the components of the source vector that contribute to polarization. Such a series is equivalent to an expansion in the mean number of scattering events and hence the name scattering expansion method. This method was originally developed for transfer computations with complete frequency redistribution in Frisch et al. (2009) and has been extended to include

(i) angle-dependent PFR in Sampoorna et al. (2011) for the non-magnetic case and in Nagendra & Sampoorna (2011); Supriya et al. (2013a) for the weak field Hanle effect, (ii) angle-averaged PFR in Sowmya et al. (2012) for the weak field Hanle effect, (iii) non-coherent electron scattering in Supriya et al. (2012), and (iv) quantum interference with angle-dependent PFR in Supriya et al. (2013b). In the present section, we extend the scattering expansion method to the problem at hand, namely, polarized line formation in arbitrary magnetic fields.

We write the source vector given in Equation (10) in the component form as

$$\begin{aligned}
S_i(\tau, x, \mathbf{n}) &= \sum_{j=0}^3 \left[(r E_{ij} + \epsilon \Phi_{ij}) B_{\nu J_b J_a} U_j + (1 - \epsilon) \right. \\
&\times \left. \oint \frac{d\mathbf{n}'}{4\pi} \int_{-\infty}^{+\infty} dx' R_{ij}(x, \mathbf{n}, x', \mathbf{n}', \mathbf{B}) I_j(\tau, x', \mathbf{n}') \right]. \quad (15)
\end{aligned}$$

In the scattering expansion method, we first compute the Stokes I by neglecting its coupling to Q , U , and V . Thus the transfer equation (1) for Stokes I reduces to

$$\mu \frac{\partial}{\partial \tau} \tilde{I}(\tau, x, \mathbf{n}) = (\varphi_I + r) \tilde{I}(\tau, x, \mathbf{n}) - \tilde{S}_I(\tau, x, \mathbf{n}), \quad (16)$$

where tilde denotes approximate values. The approximate source function is given by

$$\begin{aligned}
\tilde{S}_I(\tau, x, \mathbf{n}) &= (r + \epsilon \varphi_I) B_{\nu J_b J_a} + (1 - \epsilon) \\
&\times \left. \oint \frac{d\mathbf{n}'}{4\pi} \int_{-\infty}^{+\infty} dx' R_{00}(x, \mathbf{n}, x', \mathbf{n}', \mathbf{B}) \tilde{I}(\tau, x', \mathbf{n}') \right). \quad (17)
\end{aligned}$$

It is interesting to note that the approximations made to obtain Eqs. (16) and (17) are similar to the polarization free approximation of Trujillo Bueno & Landi Degl'Innocenti (1996). Equations (16) and (17) can now be solved using an ALI method similar to that described in Sampoorna et al. (2017). The ALI method is based on the introduction of an approximate lambda operator $\Lambda_{x', \mathbf{n}'}^*$, which is chosen to be the diagonal of the true lambda operator (see Olson et al. 1986). The ALI iterations are initiated by choosing $\tilde{S}_I(\tau, x, \mathbf{n}) = (r + \epsilon \varphi_I) B_{\nu J_b J_a}$. At each step in the iteration process, a formal solution of Eq. (16) using the short-characteristic technique of Olson & Kunasz (1987) **provides an updated** estimate of $\tilde{S}_I^{(n)}$, where the superscript (n) refers to the n th iteration step. The source function corrections $\delta \tilde{S}_I^{(n)}$ at each ALI iteration step are computed by solving a system of linear equations

$$\mathbf{A} \delta \tilde{S}_I^{(n)} = \mathbf{r}^{(n)}, \quad (18)$$

where $\mathbf{r}^{(n)}$ is a residual vector (given by the right-hand-side of Eq. (18) of Sampoorna et al. 2017). At

each depth point, $\delta\tilde{\mathbf{S}}_I^{(n)}$ and $\mathbf{r}^{(n)}$ are vectors of length $N_\lambda 2N_\mu N_\varphi$, where N_λ is the number of wavelength points in the range $[\lambda_{\min}, \lambda_{\max}]$, N_μ is the number of angle points in the range $[0 < \mu \leq 1]$, and N_φ is the number of azimuth points in the range $[0 \leq \varphi \leq 2\pi]$. Since we use diagonal approximate lambda operator, the matrix \mathbf{A} is also diagonal on the spatial grid. However, at each depth point, the matrix \mathbf{A} has the dimension of $(N_\lambda 2N_\mu N_\varphi \times N_\lambda 2N_\mu N_\varphi)$. We remark that, when angle-averaged version of $\mathcal{R}_{Q''\text{II}}^{K,K'}$ (see Eq. (14)) is used, it is possible to reduce the dimension of the matrix \mathbf{A} to $(N_\lambda \times N_\lambda)$ at each depth point, following a technique described in [Alsina Ballester et al. \(2017\)](#). Basically Eq. (17) can be expanded in terms of $\mathcal{T}_Q^K(0, \mathbf{n})$ and reduced source functions that depend only on frequency or wavelength. However, since we continue to work with Eq. (17) as it is, the size of the matrix \mathbf{A} remains the same irrespective of whether we use angle-dependent or angle-averaged version of $\mathcal{R}_{Q''\text{II}}^{K,K'}$. On the other hand, to reduce the memory requirements we avoid storing the matrix \mathbf{A} on the main memory and use secondary storage.

Clearly, solving Eq. (18) is the most time consuming part of the problem, apart from the computation of \mathbf{R}^{II} matrix and \mathbf{S}_{scat} given in Eq. (11). Traditionally, the system of linear equations represented by Eq. (18) is solved using a frequency-by-frequency (FBF) method of [Paletou & Auer \(1995\)](#), which has been generalized in [Sampoorna et al. \(2011\)](#) to handle angle-dependent PFR matrix. When the dimension of matrix \mathbf{A} is small one can use one step matrix inversion techniques such as the LU decomposition scheme (see e.g., [Press et al. 1986](#)) to solve Eq. (18). However, when N_λ , N_μ , and N_φ are large (which is required for accurate computation of the PFR matrix in the PBE regime), the FBF method becomes computationally very expensive. Therefore, here we solve Eq. (18) by an iterative method in a Krylov subspace, called the restarted generalized minimum residual (mGMRES) method originally developed by [Saad & Schultz \(1986\)](#), see also [Hubeny & Mihalas 2014](#)). For the problem at hand, with $N_\lambda = 121$, $N_\mu = 7$, and $N_\varphi = 8$ the mGMRES method is about 15 times faster than the FBF method. The ALI iterations are stopped when the maximum relative change on $\tilde{S}_I(\tau, x, \mathbf{n})$ becomes smaller than 10^{-4} .

Retaining only the contribution of I on the **right-hand-side** of Eq. (15) for the $i = 1, 2$, and 3 components of S_i , we obtain the single scattering approximation to these components as

$$\begin{aligned} [\tilde{S}_i(\tau, x, \mathbf{n})]^{(1)} &= \epsilon\varphi_i B_{\nu_j b, j_a} + (1 - \epsilon) \\ &\times \oint \frac{d\mathbf{n}'}{4\pi} \int_{-\infty}^{+\infty} dx' R_{i0}(x, \mathbf{n}, x', \mathbf{n}', \mathbf{B}) \tilde{I}(\tau, x', \mathbf{n}'), \end{aligned} \quad (19)$$

where \tilde{I} is the solution obtained by solving Eqs. (16) and (17) by an ALI method described above. In Eq. (19), $i = 1, 2, 3$ and the superscript (1) stands for single scattering. This single scattered Stokes source vector is used in a DELOPAR formal solver to obtain the Stokes parameters after the first scattering, namely $[\tilde{I}_i(\tau, x, \mathbf{n})]^{(1)}$. These Stokes parameter values are then used in Equation (15) in an iterative sequence based on the orders of scattering approach to calculate the emergent Stokes parameters. Thus, the iterative sequence for the k th scattering is given by

$$\begin{aligned} [\tilde{S}_i(\tau, x, \mathbf{n})]^{(k)} &= [\tilde{S}_i(\tau, x, \mathbf{n})]^{(1)} + (1 - \epsilon) \oint \frac{d\mathbf{n}'}{4\pi} \\ &\times \int_{-\infty}^{+\infty} dx' \sum_{j=1}^3 R_{ij}(x, \mathbf{n}, x', \mathbf{n}', \mathbf{B}) [\tilde{I}_j(\tau, x', \mathbf{n}')]^{(k-1)}, \end{aligned} \quad (20)$$

where $i = 1, 2, 3$. The iterations are stopped when the maximum relative change on the surface polarization becomes smaller than 10^{-4} (see also [Sampoorna et al. 2011](#)).

4. NUMERICAL RESULTS AND DISCUSSIONS

4.1. Atomic and Atmospheric Models

For the studies presented in this paper, we consider the atomic systems corresponding to the D₂ lines of Li I and Na I. The D₂ line results from a $J_b = 3/2 \rightarrow J_a = 1/2$ transition. The atomic parameters, such as the HFS \mathcal{A}_J and \mathcal{B}_J constants, Einstein A_{ba} coefficients, and isotope shifts are taken from [Belluzzi et al. \(2009\)](#) for the case of Li I and from [Steck \(2003\)](#) for the case of Na I. For convenience, these parameters are given in Table 1. **Note that \mathcal{B}_J for $^2\text{S}_{1/2}$ lower-level is zero.**

Figure 1 shows the level-crossing diagrams corresponding to the $^2\text{S}_{1/2}$ lower-level (top panels) and $^2\text{P}_{3/2}$ upper-level (middle and bottom panels) of ^6Li (panels (a), (b), (c)), ^7Li (panels (d), (e), (f)), and Na (panels (g), (h), (i)). The incomplete PBE regime is characterized by crossing of magnetic substates belonging to different F states, and also non-linear splitting of these magnetic components (m -states). In the case of the $^2\text{S}_{1/2}$ lower-level, level-crossings are not found in the field strength range of 0–300 G that we have considered. This validates our present approach, wherein we neglect level-crossing effects in the lower-levels, while the non-linear splitting is taken into account. In the case of $^2\text{P}_{3/2}$ upper-level, the non-linear splitting and the crossing of magnetic substates of different F states are clearly seen in the bottom panels of Fig. 1. In particular, $^2\text{P}_{3/2}$ upper level of ^6Li and ^7Li exhibit respectively, 9 and 14 level-crossings for fields in the range 0–4 G and 0–10 G, while that of Na I exhibits 14 level-crossings for

Table 1. Atomic parameters corresponding to the D_2 lines of Li I and Na I.

Isotope	Abundance (%)	I_s	λ (Å)	$A_{ba} \times 10^7$ (s^{-1})	Isotope shift (MHz)	HFS constants (MHz)		
						\mathcal{A}_J		\mathcal{B}_J
						$^2S_{1/2}$	$^2P_{3/2}$	$^2P_{3/2}$
^6Li	7.59	1	6707.90232	3.689	-10534.93	152.136	-1.155	-0.010
^7Li	92.41	3/2	6707.74416	3.689	Reference	401.752	-3.055	-0.221
Na	100.	3/2	5889.95095	6.3	-	885.810	18.534	+2.724

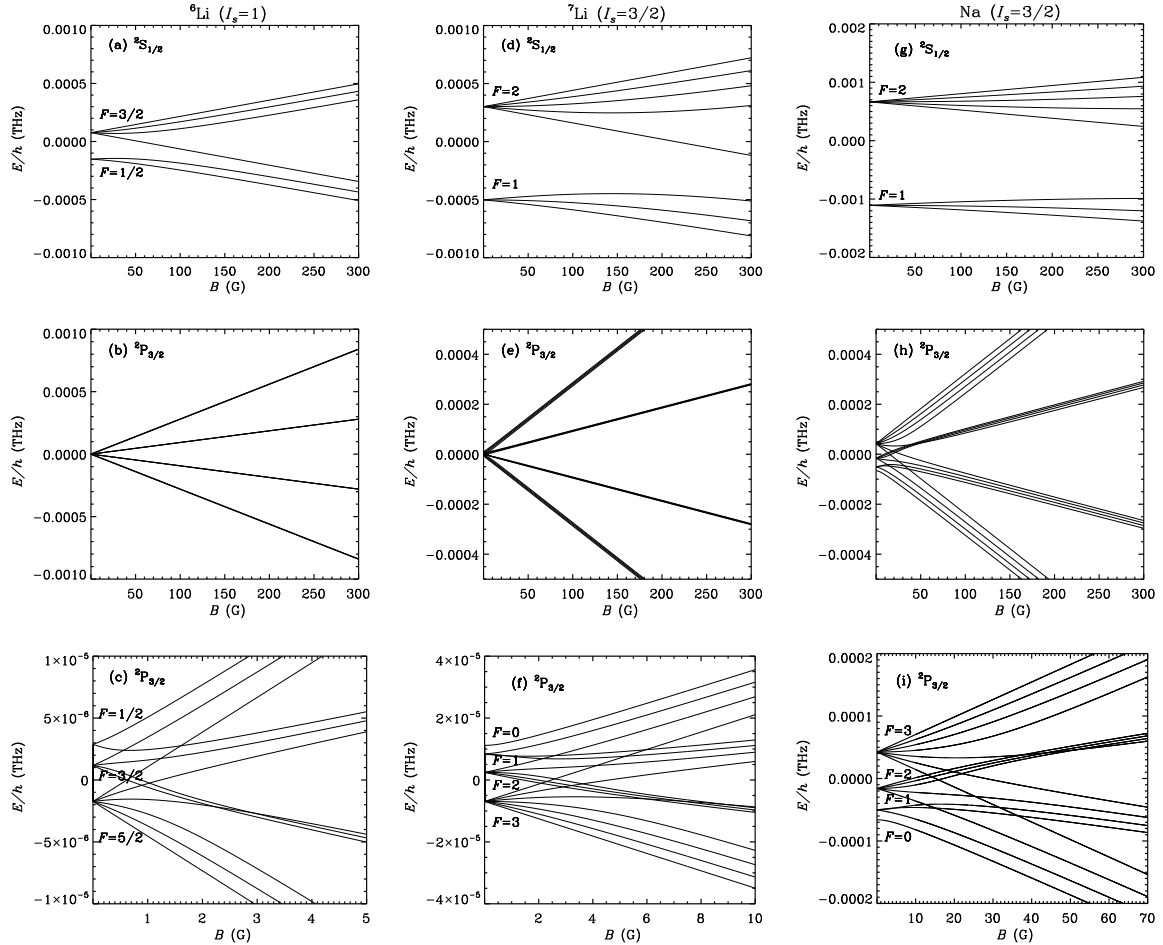


Figure 1. Level-crossing diagrams corresponding to the lower (top panels) and upper (middle and bottom panels) levels of D_2 lines of ^6Li (left column), ^7Li (middle column), and Na (right column). The bottom panels represent a zoom-in of the middle panels to clearly show the various level-crossings in the incomplete PBE regime.

fields in the range 0–50 G. For field strengths beyond the above-said range, the m -states start to bunch together indicating a gradual transition from incomplete PBE to the complete PBE regime. We recall that in

the complete PBE regime the energy eigenvectors are of the form $|J I_s m_J m_{I_s}\rangle$ and the HFS magnetic splitting varies linearly with the magnetic field strength. In the case of ^6Li and ^7Li the complete PBE regime is reached

already for fields approximately equal to or larger than 50 G (see panels (b) and (e)), while in the case of Na I it is reached for $B \geq 200$ G (see Fig. 1(h)).

We consider an isothermal planar model atmosphere, which is characterized by $(T, \Delta\lambda_D, \epsilon, r)$, where T is total optical thickness along the atmospheric normal and $\Delta\lambda_D$ is the Doppler width. In the present paper, T is defined in terms of the frequency integrated line absorption coefficient. In a solar atmosphere, D₂ line of Li I is optically thin, while that of Na I is optically thick. To study the optically thin Li I D₂ line, we consider a self-emitting slab with parameters $T = 10$, $\Delta\lambda_D = 30$ mÅ, $\epsilon = 10^{-4}$, and $r = 0$. To study the optically thick Na I D₂ line, we consider a slab with parameters $T = 10^7$, $\Delta\lambda_D = 25$ mÅ, $\epsilon = 10^{-4}$, $r = 10^{-7}$, and a lower boundary condition of $I(\tau = T, x, \mathbf{n}) = 1$. The magnetic field orientation is chosen as $\vartheta_B = 90^\circ$ and $\varphi_B = 45^\circ$. We have considered field strengths between 0 and 300 G. To reduce the computational costs, we have considered angle-averaged magnetic PFR functions for all the results we have presented (although our code can also handle angle-dependent magnetic PFR functions).

It is important to note that, although we have chosen the atomic parameters corresponding to the D₂ lines of Li I and Na I, the isothermal atmospheric models that we have considered for these two lines do not represent the corresponding solar conditions. This is particularly true in the case of Li I D₂ line. In the solar case, the line-center opacity in this line is only slightly larger than that of the continuum due to the relatively low abundance of Li I in the solar atmosphere. Thus Li I D₂ line forms at atmospheric heights corresponding to the photosphere, namely slightly above the $\tau_c = 1$ layer for the continuum at 5000 Å. Furthermore, the line opacity is expected to be significantly smaller than that of the continuum outside the Doppler core. As a result the scattering polarization signal in this line is confined to the Doppler core, which quickly drops to the continuum polarization level when moving outside the core region. This can be clearly seen in the observations presented in Stenflo et al. (2000, see also Stenflo 2011) as well as in the previous theoretical investigations based on single scattering (see Belluzzi et al. 2009; Sowmya et al. 2015). In contrast the results presented in Figs. 2–4 show significant wing polarization signal even for $B = 0$. This is because our model atmosphere for Li I D₂ line is a self-emitting slab of total optical thickness $T = 10$. Also the continuum absorption coefficient is set to zero (i.e., the parameter $r = 0$). **Furthermore, we neglect the effects of elastic collisions, despite the fact that this line forms deep in the solar atmosphere, where elastic collision rates are high.** Thus by neglect-

ing the influence of continuum and elastic collisions, the amplitudes of the wing polarization of Li I D₂ line presented in Figs. 2–4 are overestimated. However, choice of such a model atmosphere, helps in clearly bringing out the signatures of different physical mechanisms discussed in this paper, that become much more apparent when PFR and transfer effects are included. Indeed the results presented in the present paper do not aim at an accurate modeling of the scattering polarization in the solar Li I and Na I D₂ lines. **Instead, the goal of the theoretical calculations performed with isothermal slab atmospheres presented below is simply to highlight the signatures of incomplete PBE, PFR, and radiative transfer, among other effects.** Hence the Li I and Na I D₂ lines considered in this paper are only “theoretical model lines” and do not represent actual solar lines, although we continue to refer to them as Li I and Na I D₂ lines for brevity.

4.2. Theoretical Stokes Profiles of Li I D₂ Line

Figures 2–4 show the impact of magnetic fields of various strengths on the emergent Stokes profiles of a theoretical model line whose atomic parameters correspond to those of the Li I D₂ line. Figure 2 corresponds to the case of 100% ⁶Li, Fig. 3 to 100% ⁷Li, and Fig. 4 to the case of ⁶Li and ⁷Li weighted by their solar percentage abundance. Intensity shows a self-reversed emission profile, which is typical of an optically thin self-emitting slab. It remains insensitive to increase in B . This is because HFS magnetic splittings are too small compared to the Doppler width in the field strength range considered by us. Slight magnetic broadening can be seen in I for $B = 300$ G (see e.g., blue dotted line in the I panel of Fig. 2(c)). Hanle depolarization and rotation are seen in $(Q/I, U/I)$ profiles for $B \leq 50$ G (compare for example solid black and red lines in Fig. 2(b)). For $B > 50$ G transverse Zeeman effect signatures are seen in $(Q/I, U/I)$ profiles. V/I profiles show typical signatures of longitudinal Zeeman effect.

In the case of ⁷Li, the non-linear splitting of HFS magnetic components produces a slight asymmetry about the line center in the U/I profiles, for fields in the range $1 \leq B < 10$ G (see U/I panel in Fig. 3(a)). For $1 \leq B \leq 3$ G, the blue side peak in U/I is slightly higher than that on the red side. This behaviour is reversed for $B = 5$ G. For $B \geq 10$ G, the two peaks are nearly symmetric. In the case of ⁶Li, this slight asymmetry is seen only for $B = 1$ G (see dotted line in U/I panel of Fig. 2(a)). The Q/I profiles of ⁷Li show Hanle depolarization until $B \leq 5$ G (see Q/I panel in Fig. 3(a)). For $5 < B < 50$ G they tend to move towards the non-magnetic profile both in the line core as well as the wings

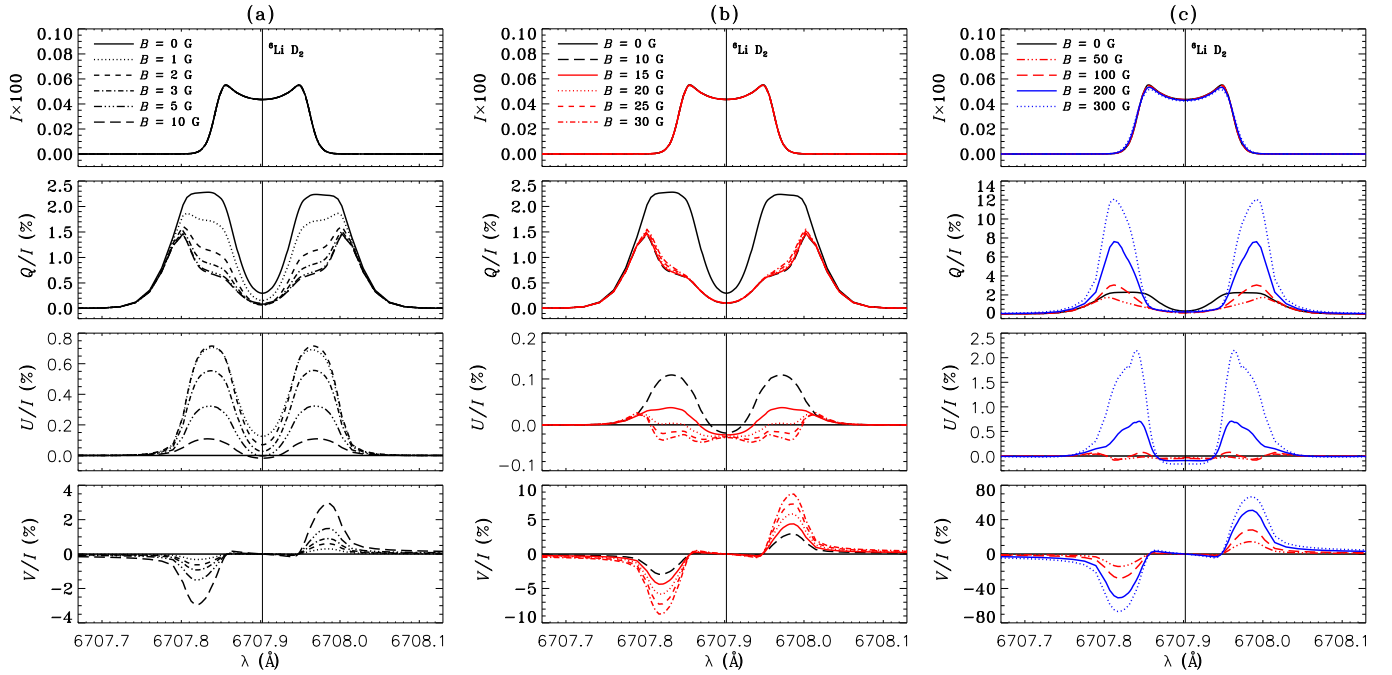


Figure 2. The emergent I , Q/I , U/I , and V/I profiles of a theoretical model line, whose atomic parameters correspond to those of the Li I D_2 line, for which 100% of the isotopes are ${}^6\text{Li}$. The line-of-sight is at $\mu = 0.11$ and $\varphi = 0^\circ$. Model parameters are $(T, \Delta\lambda_D, \epsilon, r) = (10, 30 \text{ m}\text{\AA}, 10^{-4}, 0)$. The magnetic field orientation $(\vartheta_B, \varphi_B) = (90^\circ, 45^\circ)$. The field strength is varied between 0 and 300 G.

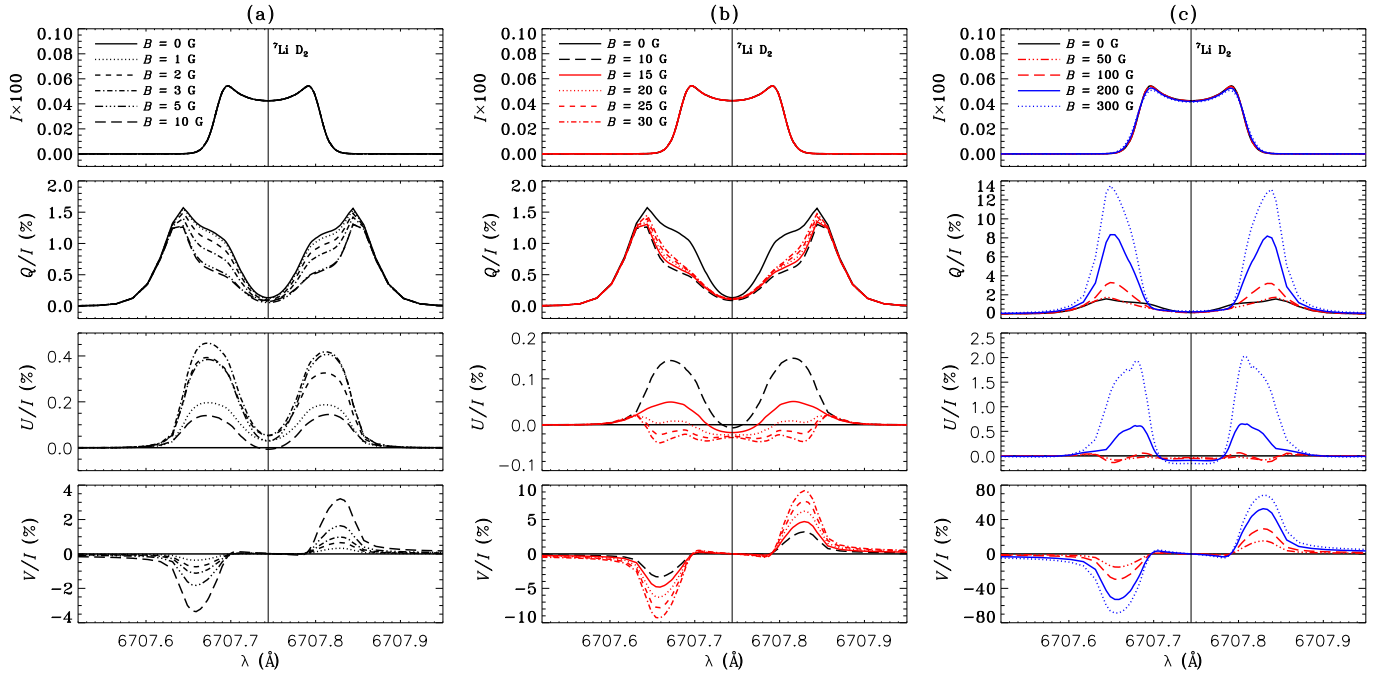


Figure 3. The emergent I , Q/I , U/I , and V/I profiles of a theoretical model line, whose atomic parameters correspond to those of the Li I D_2 line, for which 100% of the isotopes are ${}^7\text{Li}$. The line-of-sight is at $\mu = 0.11$ and $\varphi = 0^\circ$. Model parameters are $(T, \Delta\lambda_D, \epsilon, r) = (10, 30 \text{ m}\text{\AA}, 10^{-4}, 0)$. The magnetic field orientation $(\vartheta_B, \varphi_B) = (90^\circ, 45^\circ)$. The field strength is varied between 0 and 300 G.

(see Q/I panel in Fig. 3(b)). This may be attributed to level-crossing effects, although they occur only in the

range of 0 to 10 G in the case of ${}^7\text{Li}$ (see Fig. 1(f)). In the case of ${}^6\text{Li}$ this is seen clearly only in the wings of

Q/I profiles (see red lines in Q/I panel of Fig. 2(b)). The level-crossing signatures are less pronounced in the case of 100% ${}^6\text{Li}$ than in 100% ${}^7\text{Li}$ line. This is because level-crossings for ${}^2\text{P}_{3/2}$ upper level of ${}^6\text{Li}$ isotope occur at weaker fields than for the corresponding level of ${}^7\text{Li}$ isotope, as the hyperfine structure splitting is smaller for ${}^6\text{Li}$ isotope (see Table 1). Level-crossing effects can also be seen in Q/I profiles of both the isotopes of Li when combined according to their percentage abundance, particularly around the ${}^7\text{Li}$ D_2 line position (see Q/I panel in Fig. 4(b)). **It is useful to note that, for $B > 10$ G the behavior of Q/I profiles noted above could have a partial contribution from the transverse Zeeman effect, apart from level-crossings, deciphering the individual effects of these is indeed not trivial.**

Because of the isotope shift, the line center positions of the D_2 lines of ${}^6\text{Li}$ and ${}^7\text{Li}$ differ by about $160 \text{ m}\text{\AA}$, which is considerably larger than the Doppler width of $30 \text{ m}\text{\AA}$ chosen by us. Thus in Fig. 4 we see two distinct polarized line profiles in all the four Stokes parameters, apart from the blending in between the two lines modified by the radiative transfer effects. Because of the smaller isotopic abundance of ${}^6\text{Li}$, amplitude of I at the position of ${}^6\text{Li}$ D_2 line is smaller than that of ${}^7\text{Li}$. **Furthermore, the self-reversal signature found in I around ${}^6\text{Li}$ D_2 line center disappears because of reduction in total optical thickness by a factor 0.0759 in this line.** However, in polarization, ${}^6\text{Li}$ exhibits a signal which is comparable in magnitude to that of ${}^7\text{Li}$. In fact for $B = 0 \text{ G}$, Q/I at ${}^6\text{Li}$ D_2 line center is larger than that at ${}^7\text{Li}$ D_2 line center. This can also be seen clearly in the D_2 line profiles computed with 100% ${}^7\text{Li}$ and 100% ${}^6\text{Li}$ (compare black solid lines in Figs. 2 and 3). Indeed it is clearly visible in the single scattered profiles presented in Sowmya et al. (2015, see the solid line in the right panels of their Fig. 3). This can be understood using the $[W_2(J_a I_s J_b)]_{\text{hfs}}$ factor for the case of two-level atom with HFS given in the un-numbered equation at the end of p. 617 of Landi Degl’Innocenti & Landolfi (2004). Using that expression we find that $[W_2(J_a I_s J_b)]_{\text{hfs}}$ is ≈ 0.44 for ${}^6\text{Li}$ D_2 line and ≈ 0.25 for ${}^7\text{Li}$ D_2 line. Clearly $[W_2({}^6\text{Li})]_{\text{hfs}} > [W_2({}^7\text{Li})]_{\text{hfs}}$ causing larger Q/I in ${}^6\text{Li}$ D_2 line position than that at ${}^7\text{Li}$ D_2 . The transfer effects further modify this to produce the Q/I line profile shown in Fig. 4. To further clarify the influence of HFS and the impact of the relative abundance of the two isotopes, we show in Fig. 5 a comparison of non-magnetic (I , Q/I) profiles computed with (panel (b)) and without (panel (a)) HFS. When HFS is neglected, the D_2 lines of both the isotopes have $W_2 = 0.5$. Thus Q/I profiles of 100% ${}^7\text{Li}$ and 100% ${}^6\text{Li}$ are identical except for an

isotopic shift (compare dotted and dashed lines in Q/I panel of Fig. 5(a)). When the D_2 lines of these isotopes are combined according to their percentage abundance, the resulting Q/I profile shows a peak at the ${}^6\text{Li}$ D_2 line center. In the presence of HFS, the slightly larger W_2 for ${}^6\text{Li}$ D_2 line results in a dominant peak as already discussed.

The U/I profiles for $B \geq 50 \text{ G}$ (see Fig. 4(c)) exhibit an interesting behaviour at the red wing position of ${}^6\text{Li}$ D_2 line, namely that around that frequency U/I changes sign, in contrast to the corresponding case of 100% ${}^6\text{Li}$ (compare for e.g., blue dotted lines in U/I panels of Figs. 2(c) and 4(c)). To understand this we compare in Figs. 6 and 7 the (Q/I , U/I) profiles computed by including the full line absorption matrix Φ (black lines), computed by setting only $\chi_V = 0$ (blue lines), and only $\chi_Q = \chi_U = 0$ (red lines) in Φ . From Eq. (4) it is clear that anomalous dispersion coefficients χ_Q , χ_U , and χ_V couple the Stokes Q , U , and V . For the field strength regime considered in this paper only χ_V is significant, while χ_Q and χ_U are negligible for $B < 50 \text{ G}$. It is well-known that the Zeeman effect gives rise to Faraday rotation (namely it rotates the plane of linear polarization and thereby converts Q to U), which is described by χ_V (see e.g., Stenflo 1971; Rees et al. 1989). Zeeman effect also gives rise to Voigt effect (namely, it couples V to Q and U and vice versa), which is described by χ_Q and χ_U . The importance of Faraday rotation in the wings of (Q/I , U/I) profiles of optically thick lines has been demonstrated in Alsina Ballester et al. (2016, 2017, 2018), del Pino Alemán et al. (2016), and Sampoorna et al. (2017). For the optically thin Li I D_2 lines considered in this section, the Faraday rotation starts to become important in U/I for $B \geq 30 \text{ G}$ and in Q/I for $B \geq 200 \text{ G}$, while the Voigt effect starts to show up in U/I for $B \geq 50 \text{ G}$ and in Q/I for $B \geq 200 \text{ G}$. From Figs. 6 and 7 we clearly see the rotation of plane of linear polarization due to the χ_V term (compare black and blue lines), which is larger for $B = 300 \text{ G}$ than for $B = 100 \text{ G}$. The contributions of χ_U to Q and χ_Q to U are much smaller than that of χ_V (compare black and red lines). This is because χ_Q and χ_U are much smaller in magnitude than χ_V for the field strength regime considered here. Clearly, $\chi_U V$ tend to increase Q/I slightly (for $B = 300 \text{ G}$), while $\chi_Q V$ tend to reduce U/I for the field geometry chosen here. For $B = 300 \text{ G}$, U/I profiles computed with 100% ${}^6\text{Li}$ and ${}^7\text{Li}$ are positive when the χ_V term is included and negative when it is neglected (compare black and blue lines in Figs. 7(a) and 7(b), respectively). However when D_2 lines of ${}^6\text{Li}$ and ${}^7\text{Li}$ are combined according to their percentage abundance, the χ_V corresponding to ${}^6\text{Li}$ is reduced by a factor 7.59%

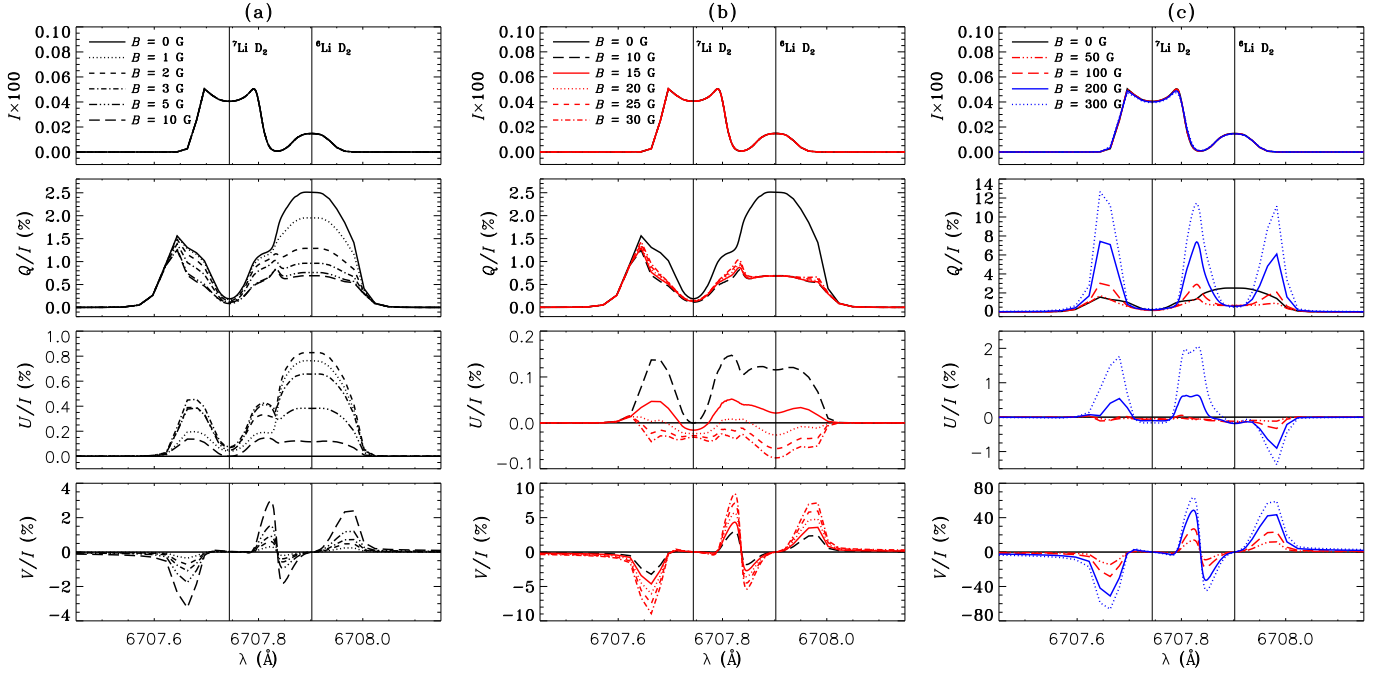


Figure 4. The emergent I , Q/I , U/I , and V/I profiles of ${}^7\text{Li}$ and ${}^6\text{Li}$ D_2 lines combined according to their isotopic abundance. Line-of-sight is at $\mu = 0.11$ and $\varphi = 0^\circ$. Model parameters are $(T, \Delta\lambda_{\text{D}}, \epsilon, r) = (10, 30 \text{ m}\text{\AA}, 10^{-4}, 0)$. The magnetic field orientation $(\vartheta_B, \varphi_B) = (90^\circ, 45^\circ)$. We recall that, these lines represent only theoretical model lines and not the actual solar lines. The field strength is varied between 0 and 300 G.

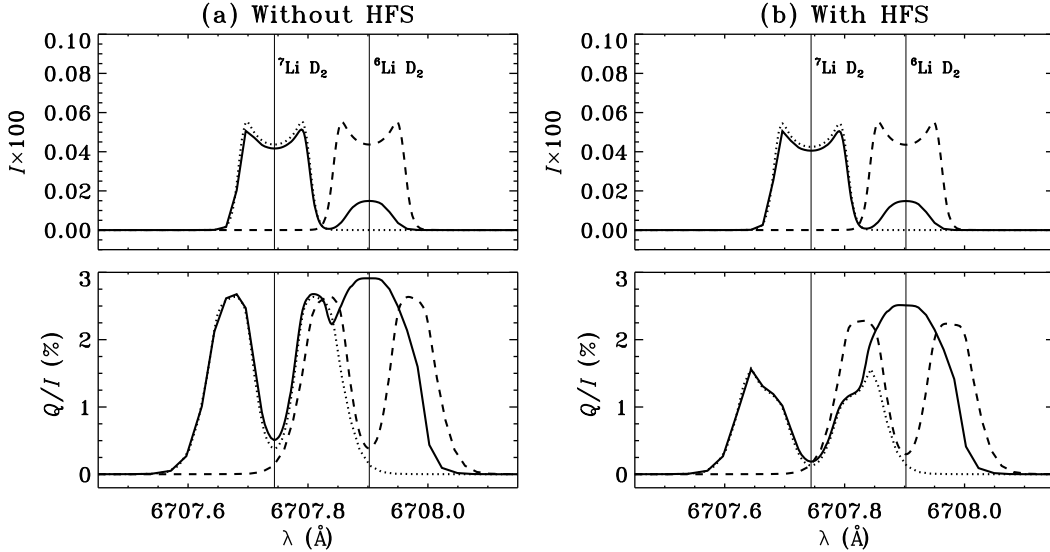


Figure 5. A comparison of $(I, Q/I)$ profiles computed with (panel (b)) and without (panel (a)) HFS in the non-magnetic case. Solid lines correspond to the combined case of ${}^6\text{Li}$ and ${}^7\text{Li}$ D_2 lines weighted by their percentage abundance, dotted lines to 100% ${}^7\text{Li}$ D_2 line, and dashed lines to 100% ${}^6\text{Li}$ D_2 line. Line-of-sight is at $\mu = 0.11$ and $\varphi = 0^\circ$. Model parameters are the same as in Figs. 2–4.

(which is the relative abundance of ${}^6\text{Li}$ isotope), thereby reducing its impact on $(Q/I, U/I)$ profiles at the red wing of ${}^6\text{Li}$ D_2 line (see e.g., Fig. 7(c)). Thus U/I at the red wing of ${}^6\text{Li}$ D_2 line continues to be negative in the combined case, in contrast to 100% ${}^6\text{Li}$ D_2 line case. Finally we note that, the impact of Faraday ro-

tation and Voigt effect on the wings of $(Q/I, U/I)$ profiles of Li I D_2 line are relatively smaller even for fields as large as $B = 100$ G (see Fig. 6). This is because we have considered a self-emitting slab of $T = 10$, wherein the transfer effects are highly reduced particularly in the wings. Faraday ro-

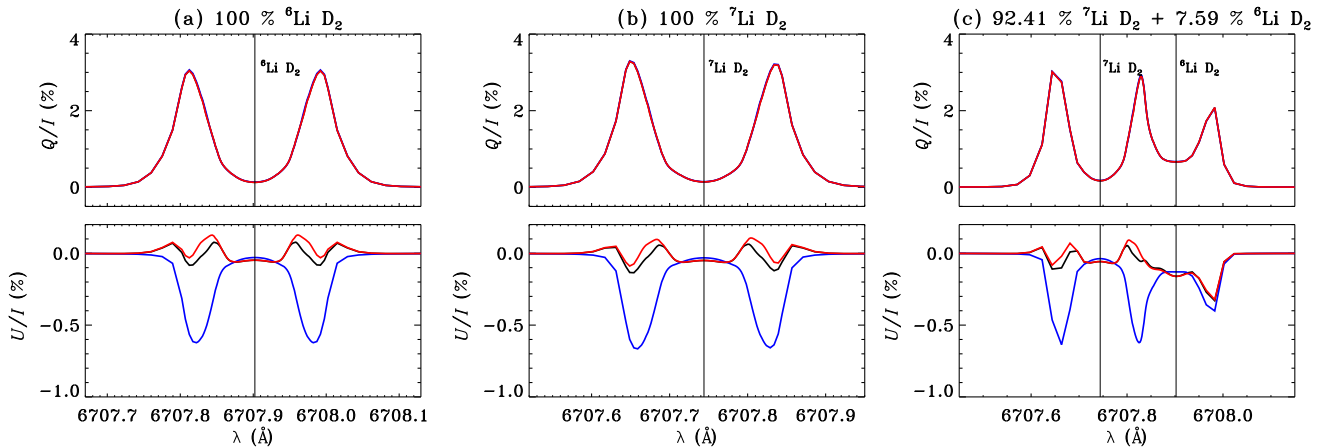


Figure 6. A comparison of $(Q/I, U/I)$ profiles computed including all the anomalous dispersion (χ_Q, χ_U, χ_V) coefficients (black lines), computed with $\chi_V = 0$ (blue lines), and with $\chi_Q = \chi_U = 0$ (red lines) for $B = 100$ G. Panel (a) corresponds to 100% ${}^6\text{Li D}_2$ line, panel (b) to 100% ${}^7\text{Li D}_2$ line, and panel (c) to the combined case of ${}^6\text{Li}$ and ${}^7\text{Li D}_2$ lines weighted by their percentage abundance. Line-of-sight is at $\mu = 0.11$ and $\varphi = 0^\circ$. Model parameters are the same as in Figs. 2–4. All the three lines coincide in the Q/I panels.

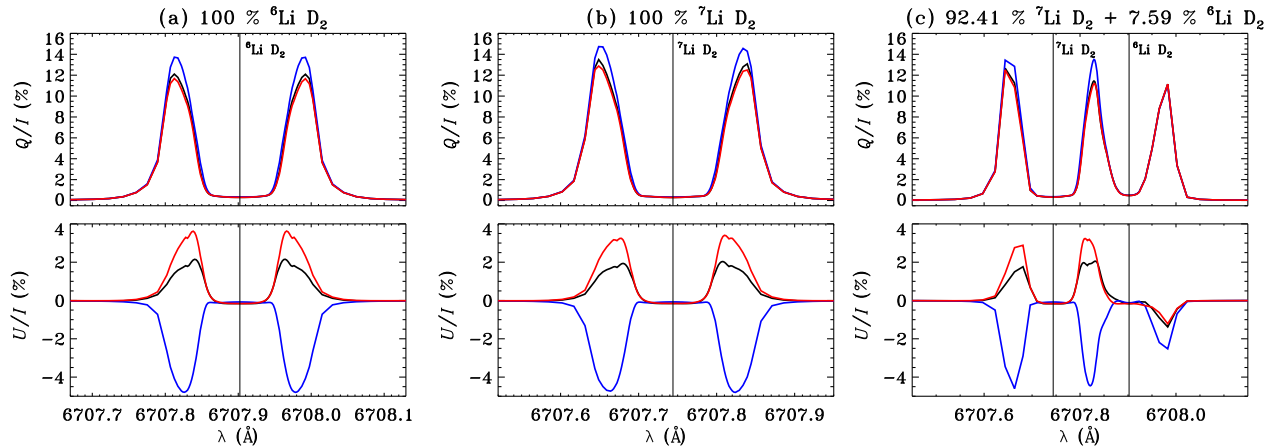


Figure 7. Same as Fig. 6, but for $B = 300$ G.

tation and Voigt effect being propagation effects would exhibit larger influence on the wings of $(Q/I, U/I)$ profiles as the optical thickness of the medium increases. They modify the non-zero wing polarization in Q/I produced by PFR. This is indeed the case for optically thick line considered in Section 4.3.

4.3. Theoretical Stokes Profiles of Na I D_2 Line

Figure 8 shows the impact of magnetic fields of various strengths on the emergent Stokes profiles of a theoretical model line whose atomic parameters correspond to those of the Na I D_2 line. For the optically thick isothermal model that we have chosen for this line, we obtain an absorption line with minima in the near wings and also broad damping wings in I , which are due to PFR. In Q/I , PFR gives rise to a line core peak, followed by the core minima, near wing peaks, and far

wing peaks for $B = 0$ (see black solid line in Q/I panels of Figs. 8(a) and 8(d)). For $0 < B < 10$ G, we see Hanle depolarization and rotation in the line core of $(Q/I, U/I)$ profiles (see Fig. 8(d)). For $10 \leq B \leq 50$ G, we see the signatures of level-crossing in the line core of $(Q/I, U/I)$ profiles, namely they tend towards the non-magnetic value (see Fig. 8(e)). For $B > 50$ G, transverse Zeeman effect signatures are seen in the line core of $(Q/I, U/I)$ profiles (see Fig. 8(f)). The Faraday rotation (Alsina Ballester et al. 2017; Sampurna et al. 2017), which results in depolarization in the wings of Q/I and generation of U/I in the wings, strongly influence the wings of $(Q/I, U/I)$ profiles for the entire field strength regime considered here. In the case of Na I D_2 line, the Voigt effect starts to show up in U/I for $B \geq 100$ G and in Q/I for $B \geq 300$ G, and its signatures are similar to those discussed in the case of Li I

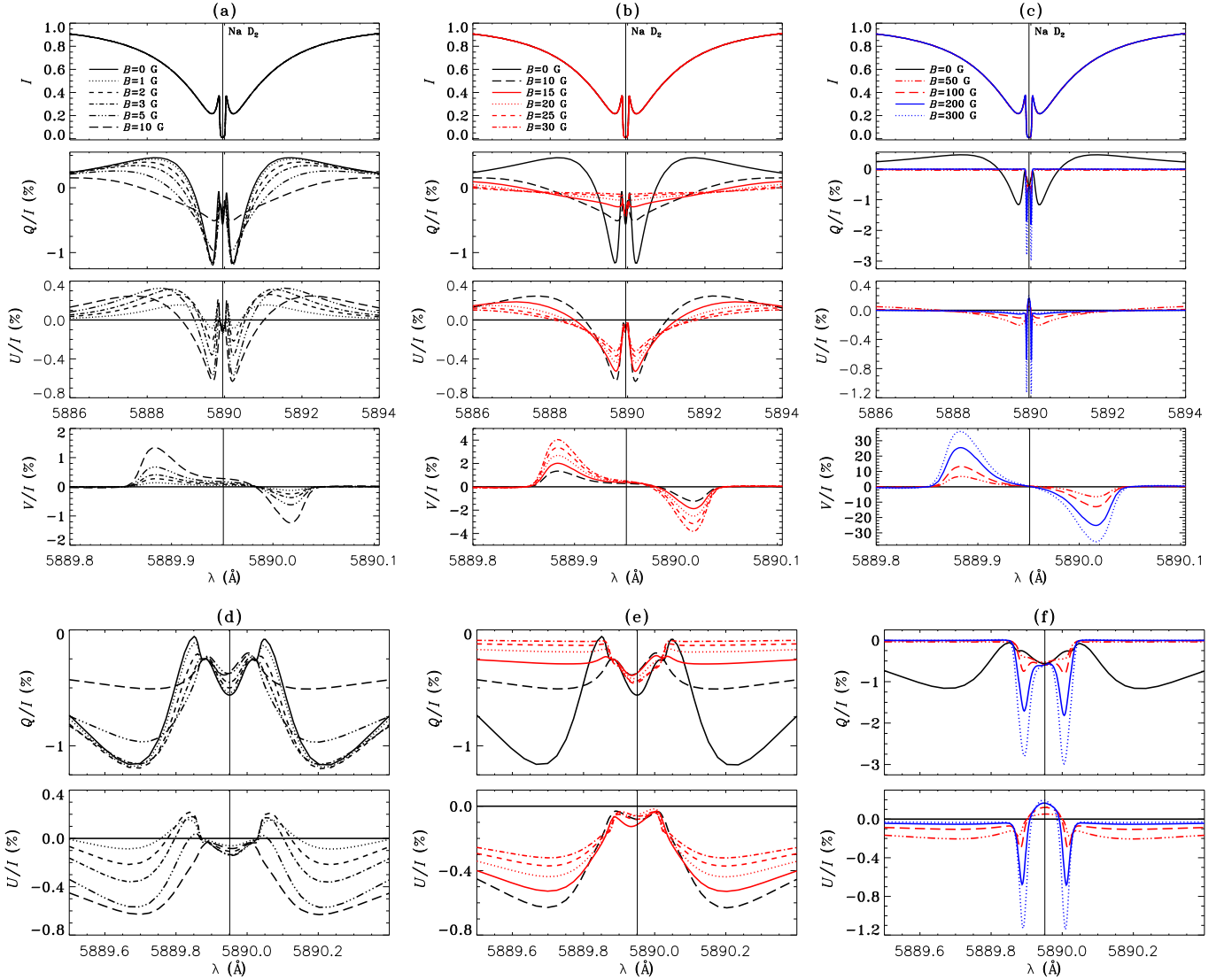


Figure 8. The emergent I , Q/I , U/I , and V/I profiles of a theoretical model line, whose atomic parameters correspond to those of the Na I D_2 line, at $\mu = 0.11$ and $\varphi = 0^\circ$ for a range of field strengths. Model parameters are $(T, \Delta\lambda_D, \epsilon, r) = (10^7, 25 \text{ m}\text{\AA}, 10^{-4}, 10^{-7})$. The magnetic field orientation $(\vartheta_B, \varphi_B) = (90^\circ, 45^\circ)$. Panels (d), (e), and (f) respectively show the magnified view in and around the line core region of $(Q/I, U/I)$ profiles shown in panels (a), (b), and (c).

D_2 lines (see Fig. 7). The influence of Faraday rotation and Voigt effect on the Stokes profiles of Na I D_2 line has been verified numerically by comparing the Stokes profiles computed with the full absorption matrix and those calculated by neglecting χ_V , χ_Q , and χ_U terms (like in Figs. 6 and 7). However, corresponding figures are not illustrated for brevity.

We note that, in the case of Na I D_2 line, the upper $^2P_{3/2}$ level is in the incomplete PBE regime for $B < 200$ G, while the lower $^2S_{1/2}$ level continues to be in the incomplete PBE regime for $B > 200$ G (see Figs. 1(g), 1(h), and 1(f)). The signatures of incomplete PBE can be clearly seen in V/I profiles, which are now asymmetric (see V/I panel in Figs. 8(a) and 8(b)). This is because of the asymmetric splitting of the mag-

netic components in the incomplete PBE regime. This results in a non-zero net circular polarization (namely $\int V d\lambda \neq 0$). The asymmetry in V/I decreases as the field strength increases beyond 30 G and the V/I profiles become more and more anti-symmetric (see blue lines in the V/I panel of Fig. 8(c)). For more details on the relation between the incomplete PBE and the non-zero net circular polarization we refer the reader to López Ariste et al. (2002). It is interesting to note that the sigma components in the Q/I profile for $B = 200$ and 300 G (see blue lines in Fig. 8(f)) are slightly asymmetric. This may be because the lower level of the D_2 line continues to be in the incomplete PBE regime.

5. CONCLUSIONS

In the present paper we have considered the problem of polarized line formation in arbitrary magnetic fields taking into account PFR in scattering on a two-level atom with HFS. To numerically solve this problem, we have extended the scattering expansion method of Frisch et al. (2009). Numerical solutions are presented by considering atomic systems representative of the D_2 lines of Li I and Na I. A range of field strengths from 0 G to 300 G are considered for our studies. This field strength range covers both the incomplete and complete PBE regimes for both Li I D_2 and Na I D_2 lines (see Fig. 1). Apart from the well-known signatures of Hanle and Zeeman effects, we have identified the signatures of incomplete PBE (namely, level-crossing, non-linear and asymmetric splitting), Faraday rotation and Voigt effects, and PFR in the Stokes profiles of the D_2 lines mentioned above, that are formed in an isothermal planar atmosphere. When compared to the single scattered Stokes profiles (see for e.g., Sowmya et al. 2014, 2015), the magnitude of the signatures of incomplete PBE regime is smaller, when radiative transfer effects are taken into account. However, radiative transfer effects need to be taken into account to accurately model the optically thick lines such as the Na I D_2 line, wherein PFR manifests itself by producing wing PFR peaks in Q/I profile, apart from the core peak. Although the signatures of incomplete PBE appear to be relatively less pronounced in the Stokes profiles formed in atmospheres where radiative transfer effects are important (in comparison with those formed in a single scattering event), it is essential to take them into account for an accurate determination of the magnetic fields using the D_2 lines of Li I and Na I considered in this paper and for other lines for which I_s is non-zero. Thus, the incomplete PBE together with Hanle and Zeeman effects must be accounted for in order to reliably use spectropolarimetric measurements of these lines as a diagnostic tool to detect the solar/ stellar magnetic fields.

We remark that in the present paper, for numerical simplicity, we have considered the academic case of isothermal planar atmospheres. To quantitatively evaluate the importance of incomplete PBE to determine solar/ stellar magnetic fields from the spectropolarimetric measurements of Li I and Na I D_2 lines, it is essential to generalize the present approach to handle realistic solar/ stellar atmospheres. However, at present this is computationally prohibitive. This is because, for an isothermal atmosphere itself, the computing time for a given magnetic field configuration (taking a single value of B , ϑ_B , and φ_B) is on the order of few days to one or two weeks depending on the optical thickness of the atmosphere. The main memory required is also substantial, being on the order of 40 to 100 GB. Although the requirement on the main memory can be somewhat reduced by avoiding storing the arrays in the main memory and using a secondary storage, reducing the CPU time requires parallelization of the code. Given this it is clear that there is still a long way to go before the present work can have practical applications as a good diagnostic tool. However the present paper certainly represents a first step in this direction. Finally, we note that, it may still be computationally feasible to apply the present work to realistic modeling. This may be achieved based on the last scattering approximation (Stenflo 1982), a sophisticated version of which has been presented in Anusha et al. (2010) for the non-magnetic case, who show that it nearly reproduces the radiative transfer solution even for optically thick lines. An attempt to generalize this so called LSA-3 approach of Anusha et al. (2010) to include arbitrary fields has been presented in Sowmya (2016).

We acknowledge the use of the high-performance computing facility at Indian Institute of Astrophysics. We thank the referee for useful comments that helped improve the presentation.

REFERENCES

- Alsina Ballester, E., Belluzzi, L., & Trujillo Bueno, J. 2016, ApJL, 831, L15, doi: [10.3847/2041-8205/831/2/L15](https://doi.org/10.3847/2041-8205/831/2/L15)
- . 2017, ApJ, 836, 6, doi: [10.3847/1538-4357/836/1/6](https://doi.org/10.3847/1538-4357/836/1/6)
- . 2018, ApJ, 854, 150, doi: [10.3847/1538-4357/aa978a](https://doi.org/10.3847/1538-4357/aa978a)
- Anusha, L. S., Nagendra, K. N., Stenflo, J. O., et al. 2010, ApJ, 718, 988, doi: [10.1088/0004-637X/718/2/988](https://doi.org/10.1088/0004-637X/718/2/988)
- Belluzzi, L., Landi Degl’Innocenti, E., & Trujillo Bueno, J. 2009, ApJ, 705, 218, doi: [10.1088/0004-637X/705/1/218](https://doi.org/10.1088/0004-637X/705/1/218)
- Belluzzi, L., & Trujillo Bueno, J. 2013, ApJL, 774, L28, doi: [10.1088/2041-8205/774/2/L28](https://doi.org/10.1088/2041-8205/774/2/L28)
- Belluzzi, L., Trujillo Bueno, J., & Landi Degl’Innocenti, E. 2007, ApJ, 666, 588, doi: [10.1086/519078](https://doi.org/10.1086/519078)
- . 2015, ApJ, 814, 116, doi: [10.1088/0004-637X/814/2/116](https://doi.org/10.1088/0004-637X/814/2/116)
- Bommier, V. 1980, A&A, 87, 109
- . 2017, A&A, 607, A50, doi: [10.1051/0004-6361/201630169](https://doi.org/10.1051/0004-6361/201630169)

- del Pino Alemán, T., Casini, R., & Manso Sainz, R. 2016, *ApJL*, 830, L24, doi: [10.3847/2041-8205/830/2/L24](https://doi.org/10.3847/2041-8205/830/2/L24)
- Fluri, D. M., Holzreuter, R., Klement, J., & Stenflo, J. O. 2003, in *ASPSCS*, Vol. 307, *Solar Polarization*, ed. J. Trujillo-Bueno & J. Sanchez Almeida (San Francisco: ASP), 263
- Frisch, H., Anusha, L. S., Sampoorna, M., & Nagendra, K. N. 2009, *A&A*, 501, 335, doi: [10.1051/0004-6361/200911696](https://doi.org/10.1051/0004-6361/200911696)
- Holzreuter, R., Fluri, D. M., & Stenflo, J. O. 2005, *A&A*, 434, 713, doi: [10.1051/0004-6361:20042096](https://doi.org/10.1051/0004-6361:20042096)
- Hubeny, I., & Mihalas, D. 2014, *Theory of Stellar Atmospheres* (Princeton, NJ: Princeton University Press)
- Landi Degl'Innocenti, E. 1984, *SoPh*, 91, 1, doi: [10.1007/BF00213606](https://doi.org/10.1007/BF00213606)
- Landi Degl'Innocenti, E., Landi Degl'Innocenti, M., & Landolfi, M. 1997, in *Proc. Forum THEMIS*, Vol. 0, *Science with THEMIS*, ed. N. Mein & S. S. Bréchet (Paris: Obs. Paris-Meudon), 59
- Landi Degl'Innocenti, E., & Landolfi, M. 2004, *Polarization in Spectral Lines* (Dordrecht: Kluwer)
- López Ariste, A., Tomczyk, S., & Casini, R. 2002, *ApJ*, 580, 519, doi: [10.1086/343111](https://doi.org/10.1086/343111)
- Nagendra, K. N., Frisch, H., & Faurobert, M. 2002, *A&A*, 395, 305, doi: [10.1051/0004-6361:20021349](https://doi.org/10.1051/0004-6361:20021349)
- Nagendra, K. N., & Sampoorna, M. 2011, *A&A*, 535, A88, doi: [10.1051/0004-6361/201117491](https://doi.org/10.1051/0004-6361/201117491)
- Olson, G. L., Auer, L. H., & Buchler, J. R. 1986, *JQSRT*, 35, 431, doi: [10.1016/0022-4073\(86\)90030-0](https://doi.org/10.1016/0022-4073(86)90030-0)
- Olson, G. L., & Kunasz, P. B. 1987, *JQSRT*, 38, 325, doi: [10.1016/0022-4073\(87\)90027-6](https://doi.org/10.1016/0022-4073(87)90027-6)
- Paletou, F., & Auer, L. H. 1995, *A&A*, 297, 771
- Press, W. H., Flannery, B. P., & Teukolsky, S. A. 1986, *Numerical recipes. The art of scientific computing* (Cambridge: Cambridge University Press)
- Rees, D. E., Murphy, G. A., & Durrant, C. J. 1989, *ApJ*, 339, 1093, doi: [10.1086/167364](https://doi.org/10.1086/167364)
- Saad, Y., & Schultz, M. H. 1986, *SIAM J. SCI. STAT. COMPUT.*, 7, 856
- Sampoorna, M., Nagendra, K. N., & Frisch, H. 2011, *A&A*, 527, A89, doi: [10.1051/0004-6361/201015813](https://doi.org/10.1051/0004-6361/201015813)
- Sampoorna, M., Nagendra, K. N., & Stenflo, J. O. 2008, *ApJ*, 679, 889, doi: [10.1086/587477](https://doi.org/10.1086/587477)
- . 2017, *ApJ*, 844, 97, doi: [10.3847/1538-4357/aa7a15](https://doi.org/10.3847/1538-4357/aa7a15)
- Smitha, H. N., Nagendra, K. N., Stenflo, J. O., Bianda, M., & Ramelli, R. 2014, *ApJ*, 794, 30, doi: [10.1088/0004-637X/794/1/30](https://doi.org/10.1088/0004-637X/794/1/30)
- Smitha, H. N., Nagendra, K. N., Stenflo, J. O., & Sampoorna, M. 2013, *ApJ*, 768, 163, doi: [10.1088/0004-637X/768/2/163](https://doi.org/10.1088/0004-637X/768/2/163)
- Smitha, H. N., Sowmya, K., Nagendra, K. N., Sampoorna, M., & Stenflo, J. O. 2012, *ApJ*, 758, 112, doi: [10.1088/0004-637X/758/2/112](https://doi.org/10.1088/0004-637X/758/2/112)
- Sowmya, K. 2016, PhD Thesis, Pondicherry University (available at IIA repository: <http://hdl.handle.net/2248/7200>)
- Sowmya, K., Nagendra, K. N., & Sampoorna, M. 2012, *MNRAS*, 423, 2949, doi: [10.1111/j.1365-2966.2012.21108.x](https://doi.org/10.1111/j.1365-2966.2012.21108.x)
- Sowmya, K., Nagendra, K. N., Sampoorna, M., & Stenflo, J. O. 2015, in *IAU Symposium*, Vol. 305, *Polarimetry: From the Sun to Stars and Stellar Environments*, ed. K. N. Nagendra, S. Bagnulo, R. Centeno, & M. Jesús Martínez González (Cambridge: CUP), 154–158
- Sowmya, K., Nagendra, K. N., Stenflo, J. O., & Sampoorna, M. 2014, *ApJ*, 786, 150, doi: [10.1088/0004-637X/786/2/150](https://doi.org/10.1088/0004-637X/786/2/150)
- Steck, D. A. 2003, *Sodium D Line Data* (Notes available at <http://steck.us/alkalidata/>)
- Stenflo, J. O. 1971, in *IAU Symposium*, Vol. 43, *Solar Magnetic Fields*, ed. R. Howard, 101
- Stenflo, J. O. 1982, *SoPh*, 80, 209, doi: [10.1007/BF00147969](https://doi.org/10.1007/BF00147969)
- Stenflo, J. O. 1994, *Solar magnetic fields - Polarized radiation diagnostics* (Dordrecht: Kluwer)
- Stenflo, J. O. 2011, in *Astronomical Society of the Pacific Conference Series*, Vol. 437, *Solar Polarization 6*, ed. J. R. Kuhn, D. M. Harrington, H. Lin, S. V. Berdyugina, J. Trujillo-Bueno, S. L. Keil, & T. Rimmele, 3
- Stenflo, J. O., Keller, C. U., & Gandorfer, A. 2000, *A&A*, 355, 789
- Supriya, H. D., Nagendra, K. N., Sampoorna, M., & Ravindra, B. 2012, *MNRAS*, 425, 527, doi: [10.1111/j.1365-2966.2012.21497.x](https://doi.org/10.1111/j.1365-2966.2012.21497.x)
- Supriya, H. D., Sampoorna, M., Nagendra, K. N., Ravindra, B., & Anusha, L. S. 2013a, *JQSRT*, 119, 67, doi: [10.1016/j.jqsrt.2012.12.016](https://doi.org/10.1016/j.jqsrt.2012.12.016)
- Supriya, H. D., Smitha, H. N., Nagendra, K. N., Ravindra, B., & Sampoorna, M. 2013b, *MNRAS*, 429, 275, doi: [10.1093/mnras/sts335](https://doi.org/10.1093/mnras/sts335)
- Trujillo Bueno, J. 2003, in *ASPSCS*, Vol. 288, *Stellar Atmosphere Modeling*, ed. I. Hubeny, D. Mihalas, & K. Werner (San Francisco: ASP), 551
- Trujillo Bueno, J., & Landi Degl'Innocenti, E. 1996, *SoPh*, 164, 135, doi: [10.1007/BF00146629](https://doi.org/10.1007/BF00146629)